A design method for rock groynes exposed to overtopping from long-period ship wave loads

Arne Seemann[1], Gregor Melling[1], Hanne Jansch[1] and Bernhard Kondziella[1]

Abstract

In German estuaries ship-induced loads have increased in recent years due to the gradual change of the fleet structure towards bigger vessels. Groynes in particular are vulnerable to long-period primary ship wave loading due to an overtopping phenomenon which at some localities leads to severe damages. While in recent years the hydraulic processes have been the focus of investigations, currently no rock sizing method exists for this special load case.

To develop a design method and to better understand the processes leading to groyne erosion, the data from a previously conducted prototype experiment with two groynes is analysed in this paper. The prototype experiment was carried out over several years and was accompanied by a comprehensive monitoring, consisting of wave and current measurements as well as laser scan surveys.

Relationships of primary wave heights, overtopping flow conditions and rock movements are investigated. Making use of similarities to weir flow and overtopped riprap embankments, existing analytical and empirical formulae are applied to this problem and evaluated. Important influencing factors like the ambient water level are discussed. Ultimately, using the Thornton et al. (2014) stability function the majority of observed erosion events could be predicted correctly with only a small number of false detects. On this basis, a workflow for the stone sizing of rock groynes exposed to long-period ship waves is formulated.

Keywords

Ship waves, rock groynes, long-period wave overtopping, empirical and analytical equations, stone size prediction, field survey

1 Introduction

The effect of ship-generated waves on waterway embankments has routinely been studied for inland waterways with narrow and constant cross-sections and is documented in well-known guidelines (GBB 2010; CIRIA 2007). Less attention has been paid to the ship-induced wave and current loading in more complex bathymetries like coastal waterways and estuaries, as naturally occurring loads have often been dominant in the past. However, the hydrodynamic loads induced by ships have steadily increased and have become highly relevant in coastal waterways, due to the growing dimensions

of sea-going ships. The waves generated by ships can be separated in two main systems. A low frequency primary wave and a high frequency secondary wave system (Bertram 2002). The secondary wave system consists of high frequency transversal and divergent waves, originating due to pressure disturbances at the bow and the stern (Soomere 2007). The primary wave system is a long-period depression wave system, which is forced by the moving displacement volume of the vessel (Bhowmik et al. 1982). Other components of the primary wave system are the preceding bow wave and the subsequent stern wave (Schiereck 2001). The height distance from the depression (also called drawdown) to the stern wave is sometimes called surge (Houser 2011). However, in this paper it is referred to as primary wave height, in accordance with Melling et al. (2021). Especially in regions with large vessels and narrow, confined waterways, the long period wave components are reported to have a significant impact on shallow area morphology (Schoellhamer 1996; Schroevers et al. 2011; Rapaglia et al. 2015) and shoreline morphology (Zaggia et al. 2017; Muscalus and Haas 2022). In areas with extensive shallow areas adjacent to the shipping channel, a specific transformation of the primary wave system can be observed, where the previously V-shaped depression wave becomes asymmetric, with a steep bore-like primary wave (Parnell et al. 2015). However, this pattern differs significantly from the primary wave transformation observed at transversal groynes, which is the phenomenon discussed in this paper.

The interaction with groynes is characterized by energy transformation, as the initial velocity of the primary wave is decreased at the structure and the kinetic energy is transformed into potential energy, leading to an increase in primary wave height of up to 2.5 times the initial wave height at the groyne tip. The same mechanism is described for bore-like tsunami waves overtopping coastal structures (Esteban et al. 2017). Wave focusing and reflection processes also have an influence, resulting in a higher wave height at the groyne root. It is these effects which give rise to potentially damaging wave-structure-interaction at the groyne, in which high-velocity, turbulent flows develop on the crest and lee-side groyne slope due to an overflowing surge. This is the reason that groynes are particularly susceptible to being damaged by long-period primary ship wave loads (Melling et al. 2019, 2021). Figure 1 shows this interaction at Juelssand in the Lower Elbe, Germany. At first, the drawdown emerges leading to a water level depression and a return current around and over the groyne (Figure 1 a-c). After the drawdown is fully developed, the current turns and the primary wave unfolds, eventually starting to severely overflow the groyne (Figure 1 d-f). As indicated by the timestamps, the overtopping flow persisted for approximately 20 s in this representative example. The resulting typical damage pattern starts with an initial erosion on the lee-side slope followed by deterioration of the groyne crest and the root section (Figure 1, right).

Figure 1: Left: Example of ship wave interacting with the groyne at Juessand; a) ship approaching, bow wave b) return current and drawdown emerges with slight overtopping over the groyne c) full return current with upstream overtopping over the groyne d) maximum drawdown e) stern wave arrives f) stern wave-induced overflowing (Melling et al. 2021). Right: Typical damage associated with primary wave overtopping.

There are few publications looking into the effect of primary ship waves on rock structures stability in coastal waters (Dempwolff et al. 2022). There are stone sizing equations created for secondary wave attack (Verhey and Bogaerts 1989) and secondary wave combined with river flow (Kurdistani et al. 2019), as well as design guidelines for bank protection

of inland waterways (GBB 2010; CIRIA 2007). However, the groyne loads created by vessels are fundamentally different from typical primary or secondary waves attacking along channel embankments. Also, commonly used design methods for rock armour structures against wind waves (e.g. van der Meer 1988) are not applicable due to the same reason.

With the typical damage at the groynes occurring on the leeward slope of the groyne, it has been observed that the primary wave overflowing process is responsible for the erosion. There has been much research on the prediction of the stability of riprap or rockfill exposed to overflowing loads. In a literature review Abt et al. (2013) found 21 relationships which were developed for general or specific applications. These formulae can be categorized into empirically and analytically derived formulas. Empirically derived formulas have the downside to only be accurate for the range of applicability of the experiments through which they were derived. Analytical formulas, however, are assumed to understand the essential physical processes behind a given phenomenon and thus to provide better predictions, even outside of test boundaries (Pells and Peirson 2015). However, Khan and Ahmad (2011) indicate that uniform flow and tractive shear stress approaches cannot be applied for shallow flows over large rough elements. Hence, standard analytical flow and sediment transport formulas cannot be utilized in these conditions. With the availability of a large enough dataset, Khan and Ahmad (2011) recommend fully empirical formulas as the best way to approach this problem.

To this date, the local waterway authorities and consulting engineers rely on practical experience in the design and assessment of groynes which are subject to overtopping primary waves. In the absence of guidance, a major research program was initiated by the Federal Waterways and Engineering and Research Institute and local waterway authorities in Germany. Two optimized groyne designs were developed and evaluated in a prototype field experiment, which featured a recessed and a reinforced root section. This field experiment is documented in Melling et al. (2021), in which the wave structure-interaction and the measured data are described. However, what is still missing is an in-depth data analysis to understand the quantitative relationships of the damage mechanism and to allow future predictions of groyne stability based on this data. This is what determines the main aims of the paper at hand:

- Understand the observed erosion in relation to the primary ship wave and identify and quantify influencing factors.
- Develop a stone sizing workflow for groynes exposed to long period ship waves.

To meet these aims, an analysis of the Juelssand groyne field experiment data (Melling et al. 2021) was performed. To identify and quantify the important parameters of the overflow phenomena and the stability of the riprap, existing empirical and analytical formulae from comparable problems in hydraulic engineering were utilized.

The paper is structured as follows. The field experiment and data are briefly described in Section 2.1, followed by a review of existing formula concerning weir overflow, rough bed flow and riprap stability in Sections 2.2 and 2.3. The actual analysis is presented in Section 3, in which the characteristics of the wave are related to the overflow discharge, the ambient water level and the observed erosion. In Section 4 the results, underlying assumptions and uncertainties are discussed. Furthermore, a stone sizing workflow is presented and its applicability and limitations are debated. Finally, the conclusions are laid out in Section 5.

2   Data and methods

2.1 Prototype field data

This paper conducts an analysis of the data gathered in a field experiment documented in Melling et al. (2021). A brief description of the experiment and the data is given to provide context to the reader.

To enhance the resilience of rock groynes against load from overflowing primary ship waves, two optimized designs were developed and built at prototype scale in the Lower Elbe Estuary (Figure 2). Both prototype groynes have side slopes of 1:4, a head slope of 1:5, a slight longitudinal inclination of 1:77 and a groyne height of approximately 2 m. The shape of the groyne crest is rounded. The difference between the two designs resides in the shape of the root area. The first groyne (B29) has a recessed root area with a width of 25 m, which is meant to allow wave energy to bypass the structure. The second design (B31) has a reinforced root area in the form of a broadened and rounded transition area with a radius of 25 m to the bank revetment. This feature is meant to reduce wave focussing and strengthen the root area.

Figure 2: Groyne geometries used in the prototype experiment. Left: B29 with recesed root area. Right: B31 with reinforced root by broadened and rounded transition area to the bank revetment (Melling et al. 2021).

At the beginning of the test, both groynes were built with a standard rock grading of $CP_{90/250}$ with high-density iron-silicate rocks with a density of ~3.7 t/m^3, analogous to the existing conventional groynes at this site. At a later date, after an interim evaluation of the groyne conditions, the B29 was rebuilt using a coarser rock grading of $LMB_{5/40}$. This variant is hereafter referred to as B29 V2. The thickness of the riprap layer is for all versions specified as two times D_{50}. The core of the groynes body consists of the remnants of older groynes and was considered impermeable.

Table 1: Specific parameters of rock grading classes which were used in the prototype experiment. These are mean valus from several inspection reports provided by the manufacturer (accessible: https://www.aurubis.com/peute/downloads). D_{50} is the median sieve diameter, C_u the coefficient of uniformity, which are calculated from the reported rock gradings. ρ_s is the stone density.

Rock grading	D_{50} [cm]	C_u [−]	ρ_s [t/m^3]
$CP_{90/250}$	15	1.5	3.7
$LMB_{5/40}$	20	1.5	3.7
$LMB_{10/60}$	24	1.3	3.7

This experiment was accompanied by a monitoring with the following components (see Figure 3):

- Wave measurements using pressure gauges; each groyne 5 positions (P1-P6)

- Flow velocity measurements using an acoustic doppler velocimeter (ADV), only deployed on recessed groyne B29 V2

- Armour layer surface surveys using pile-mounted terrestrial laser scanners

- AIS data providing vessel and nautical parameters for every wave event

The pressure gauges were deployed along defined cross-sectional profiles. For B29 the middle cross-section is crucial, since the root cross-section is located in the recess and thus not adversely affected by overtopping. The location of the gauges was optimized for measuring wave events from outbound ships, which at this site sail closer to the groynes and thus generate larger primary waves. Accordingly, gauges P4 and P5 are located on the wave-facing side in the root cross-section. Conversely, for outbound events no information was gathered on the leeward side of the measurement cross-sections.
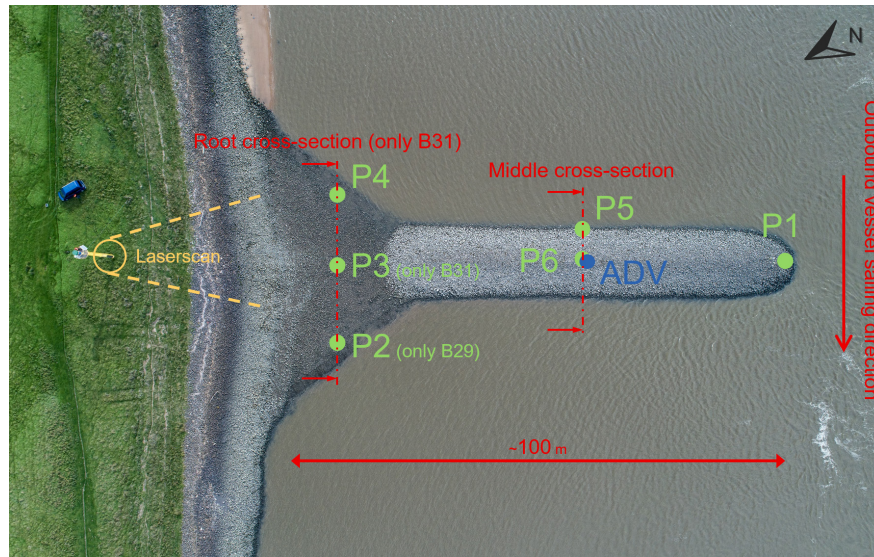
Figure 3: Location of pressure sensors (P1-P6), current meter (ADV) and laser scanner illustrated at B29 V2 (recessed groyne). The sensors were deployed in a middle and root cross sections, which are used in further calculations. The root cross section is only considered for the B31.

The pressure sensors and laser scanner were continuously operating the majority of the time shown in Table 2, except for longer periods of down time during the winter months. For B29 V2 an ADV was deployed on the groyne crest along the middle cross-section. The ADV records the flow velocity components approximately 20 cm above the groyne crest. For the quantification of the spatial and temporal riprap layer deformations laser scanner surveys were used. In order to record most of the surface, the groyne was scanned automatically at every low tide. However, surveying rough wet rock surfaces with a terrestrial laser scanner at low angles in a remote coastal environment adjacent to a major shipping channel poses a number of challenges for the equipment, recording and post-processing of the data. For this reason, numerous scans had to be discarded, leading, at times, to bigger time gaps between consecutive scans.

Table 2: Measurement periods, present rock grading and available data

Groyne number	Measurement cross-section	Monitoring period	Rock grading class	Pressure sensors	Laserscan	ADV
B31	Middle, Root	2015 – 2017	$CP_{90/250}$	x	x	-
B29 V1	Middle	2015 – 2016	$CP_{90/250}$	x	x	-
B29 V2	Middle	2017 – 2019	$LMB_{5/40}$	x	x	8 months

Figure 4 shows a brief overview of the vessel related parameter and the corresponding wave information at the groyne tip for the measurement period B29 V1. In this time period 7231 wave events were recoded. The time from drawdown to stern wave is plotted as a proxy for the primary wave period, as this value were not processed from the raw data. The median time is ~60 s, which suggests very long and gentle primary waves. The huge spread and the extreme values in the time are due to faulty automated processing. The suggested mean primary wave period is about 120 s. Further description and visualization of the data at both groynes can be found in Melling et al. (2021).
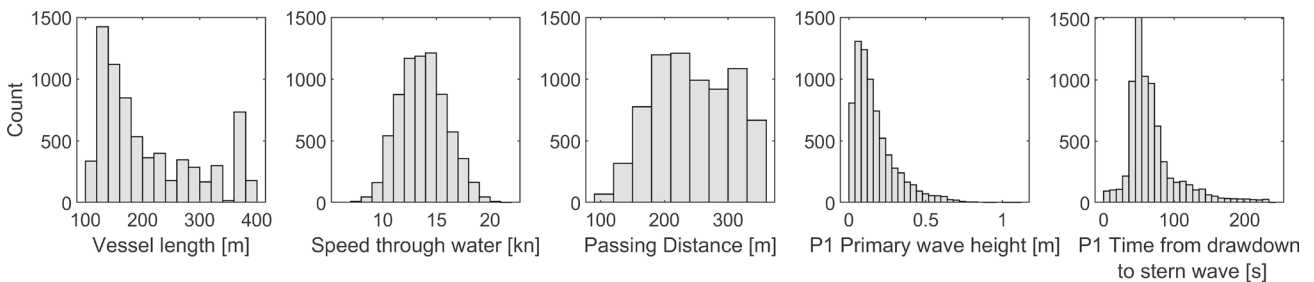

Figure 4: Selected data overview for relevant time period of B29 V1 (c.f. Table 2) (n=7231). Primary wave height and the time from drawdown and stern wave was measured at the groyne tip. The passing distance is also related to the groyne tip.

2.2 Formulas describing hydraulic loads on groynes

Figure 5 shows a conceptual model of a groyne overflowing event derived from observations of wave-structure-interaction. The relevant variables that will be used in further analysis are denoted in the figure and described in following section.
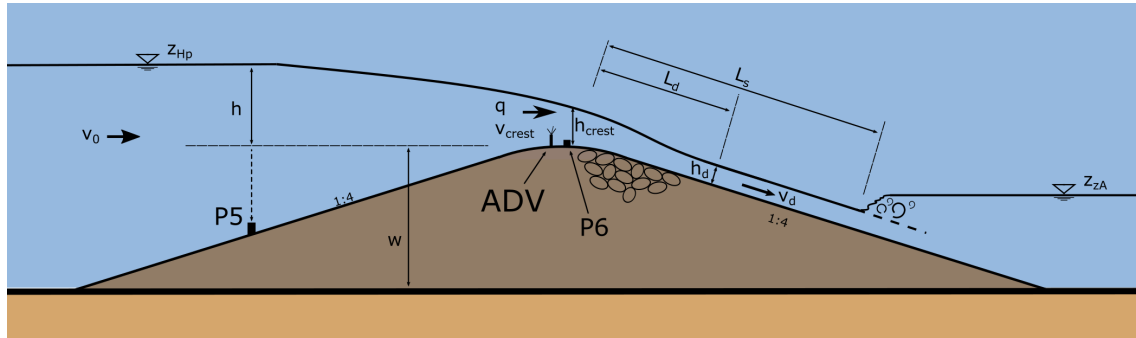

Figure 5: Load case of primary wave overflowing event at maximum elevation of the wave. The measurement gauges from the middle cross-section of B29 V2 are displayed.

The hydraulic head in front of the groyne is denoted by h, the flow depth over the groyne crest as h_{crest}, the overflowing unit discharge as q, the flow velocity over the groyne crest as v_{crest}, the approach flow velocity v_0 and the length of the free-flowing leeward slope L_S. On the leeward slope, flow depth and the velocity of the fully developed rough bed flow are denoted as h_d and v_d. L_d represents the flow length required for a fully developed boundary layer in rough bed flow. The water level elevation of the primary wave and the drawdown are denoted as z_{Hp} and z_{zA}. The groyne height is labeled as w.

At first glance, the similarity with flow over weir structures is apparent. Therefore, weir overflow theory and relevant formulae will be briefly presented in the following.

The first description of weir flow was formulated by Poleni in 1717 (Peter 2005).

$$Q = \frac{2}{3}\mu_P \cdot b \cdot \sqrt{2g} \cdot h^{\frac{3}{2}}$$

(1)

where b is the width of the weir, h is the upstream hydraulic head and μ_P is the empirical weir coefficient. In this model all physical deviations and unknown processes are summarized in this empirical coefficient.

Numerous investigations have calculated the empirical coefficient μ_P for a variety of different weir geometries and hydraulic conditions. Influence factors that are combined in this parameter include the structure geometry, the downstream water level, oblique approach flow, roughness and the presence of piles (Aigner 2008; Pařílková et al. 2012). However, this simple model can lead to the phenomenon that μ_P can be dependent on the hydraulic head itself (Peter 2005). A more sophisticated version of this formula is from du Buat (Peter 2005), which also includes the kinetic energy yielded by the approach velocity v_0 (see Figure 1). However, this parameter was not measured in the monitoring described in section 2.1 and thus cannot be used. Hence, for the following analysis the Poleni equation was selected. The Poleni formula describes the discharge for free flow conditions. The free weir flow relates to a change in the flow regime from subcritical to supercritical flow over the weir structure, which can be expressed by the means of the depth related Froude number. The described methods apply to stationary conditions at weir structures. The overflowing process of primary ship waves however is a dynamic and time dependent process. Therefore, the applicability of this formula to the conditions at the groynes has to be investigated and evaluated using the prototype data.

As stated in section 2.1, no flow depth or velocity was measured on the leeward slope of the groyne (with respect to outbound ships, see Figure 3). Thus, the flow processes on the leeward side slope are unknown. Yet, these processes determine the maximum stress on the riprap of the groyne and have to be considered. To approximate the flow velocity and depth the Manning formula eq. (2) with Strickler coefficient for riprap eq. (3) are used.

$$v_d = k_s \cdot R_h^{2/3} \cdot S^{1/2}$$

(2)

here, v_d is the average velocity for a fully developed flow. The hydraulic R_h radius is suggested to be the flow depth h_d in present case, S is the inclination of the slope and k_s the Strickler coefficient.

$$k_s = \frac{b_1}{k^{b_2}}$$

(3)

The Strickler coefficient is based on values of $k = S \cdot d_{50}$, $b_1 = 12.21$ and $b_2 = 0.159$ for crushed dumped rocks according to Abt et al. (1987).The flow depth and the corresponding velocity are calculated iteratively based on the given discharge.

In the case of overflowing groynes, the exposed slope length on the lee side L_S (cf. Figure 5) is constrained by the water level in the lee-side groyne field. To estimate the degree of acceleration experienced by the flow on the lee slope, the degree of rough bed flow development has to be considered. In an investigation about rock chutes Platzer (1983) determined the following relationship between turbulent boundary layer thickness δ, flow length x, roughness height k, as well as the slope angle α:

$$\frac{\delta}{x} = 1.65 + 0.4 \cdot \tan\alpha \cdot \frac{x}{k} \pm 0.4$$

(4)

This equation can be used to calculate the point on the slope where the turbulent boundary layer intersects the water surface and thus full turbulent flow emerges and the entrainment of air into the flow starts. For the following analysis it is assumed that at this point the rough bed flow is fully developed. In order to make this formula applicable to the present case, it was rearranged and converted into the nomenclature from Figure 5. In accordance with the previous assumptions the terms $R_h = h_d = \delta$ and $L_d = x$ are applied to the formula. The uncertainty term ±0.4 is neglected and the formula is rearranged into L_d, resulting in eq. (5):

$$L_d = \frac{1}{8} \cdot \cot\alpha \ (20h_d\text{-}33k)$$

(5)

In comparison with the observed slope length L_S, it can be determined whether fully developed rough bed flow is present or not.

2.3 Formulas for rock sizing against overflowing riprap

Abt et al. (2013) reviewed 21 formulas concerning the stability of riprap against overtopping flow. Furthermore, they tested each formula using a dataset containing a variety of laboratory experiments. The performance of each formula was evaluated for different stone size classes. The best performing formula are used in this paper to evaluate the erosion of rock groynes which are exposed to overtopping flow.

Abt et al. (2013) found that the formula of Khan and Ahmad (2011) was the best performing equation across the entire range of stone sizes:

$$D_{50} = 0.66 \ t^{0.58} S^{0.22} C_u{}^{-0.45} q_c{}^{0.21}$$

(6)

This is a general purpose formula, based on a full regression model that was developed with the data of Robinson et al. (1998) and Abt and Johnson (1991) with 51 data points.

The best performing equations of the intermediate stone size band (5 cm $\leq D_{50} \leq$ 25 cm) are of special interest, as they reflects the rock size used groyne prototype (see Table 1). Among them is the formula of Olivier (1967), who investigated flow running through and over rock fill dams. The formula is based on the tractive shear equation:

$$D_{50} = 1.749 \cdot q_c^{\frac{2}{3}} \left[\frac{\rho_s - \rho_w}{\rho_s} \right]^{-\frac{10}{9}} S^{\frac{7}{9}}$$

(7)

Where, q is the unit discharge in [ft^2/s], d_s is the equivalent stone diameter in [ft] and S the downstream slope inclination.

Abt and Johnson (1991) developed a regression-based stability expression for application in waste impoundment encasement based on physical experiments:

$$D_{50} = 5.23 \cdot S^{0.43} q_{design}^{0.56}$$

$$\text{with } q_{design} = 1.35 \, q_c$$

(8)

where, S is the slope gradient and q [ft^2/s] the discharge at failure of the riprap.

Chang (1998) used an analytical threshold of motion approach combined with a reanalysis of experimental data for the development of the relationship:

$$D_{50} = \frac{0.887 \cdot q_c^{\frac{5}{9}}}{S^{5/18} \cdot \left[\frac{1}{S} - \frac{1}{\tan(1 + 5S)\phi}\right]^{25/27}}$$

(9)

In this formula q and S are the failure unit discharge and the slope gradient, and ϕ is the angle of repose of the riprap.

The good performance of the formula from Khan and Ahmad (2011) inspired Thornton et al. (2014) to follow the idea of a full empiric regression approach. The novelty in Thornton et al. (2014) was the implementation of the specific stone gravity as predictive parameter. Furthermore, the underlying dataset was increased, widening the band of validity:

$$D_{50} = 0.57 \, S^{0.20} C_u^{-0.28} q_c^{0.21} t^{0.62} \left[\frac{1.16}{(\rho_s - 1)^{0.30}}\right]$$

(10)

In this formula, S is the slope inclination, C_u the coefficient of uniformity, t the riprap layer size in nD_{50} and q_c the failure unit discharge. This model is based on 102 data points.

All of these formulas use the discharge as the hydraulic input parameter and are therefore only valid for fully developed rough bed flow. This has the advantage of having a flow resistance formula directly built in the stability equation without an intermediate step to calculate flow velocities or shear stress. Furthermore, no arbitrary definitions of the riprap surface level and hence the flow depth have to be made (Hiller et al. 2018). On the other hand, formulas with the flow velocity as an input parameter have the advantage, that they do not require fully developed flow conditions to be applicable. A flow resistance formula (e.g. Manning equation) is needed to calculate the flow velocity from a known discharge and slope geometry. Two of the latter type of equations are presented in the following.

Isbash (1936) was the first to formulate a stability equation for the construction of rock fill dams. The work is based on prototype-scale experiments of stones dumped into flowing water:

$$D_{50} = \frac{v_c^2}{2g \cdot Y^2} \left(\frac{\rho_s}{\rho_s - \rho_w}\right)$$

(11)

In this formula the empirical constant Y is introduced, which varies for different turbulence regimes.

Hartung and Scheuerlein (1970) expanded on the work of Isbash (1936), by investigating the influence of the air entrainment into the flow. They introduced an aeration factor σ and considering the influence of the sloped angle $\cos\varphi$:

$$D_{50} = 0.69 \frac{v_c^2}{2g \cdot \cos\varphi} \left(\frac{\sigma \cdot \rho_s}{\rho_s - \rho_w}\right)$$

$$\text{with } \sigma = 1 - 1.3\sin\alpha + 0.08\frac{y_m}{\theta_m}$$

(12)

In this formula θ_m is he mean roughness height, α the slope angle and y_m the mean flow depth.

Three of all seven presented equations do not include a term for the specific rock density. These equations are developed for quarried rock with rock density around 2.65 t/m^3 (Abt et al. 2013). However, as shown in Table 1, the rocks in place have a ρ_s around 3.7 t/m^3. To adjust the diameter of those formulas, eq. (13) is used. It is derived by equalizing buoyant gravity forces of initial ρ_s stone and a target ρ_s stone (Gier and Schüttrumpf 2012).

$$\vartheta = \left(\frac{\rho_{min} - \rho_w}{\rho_s - \rho_w}\right)^{\frac{1}{3}}$$

(13)

Here, ρ_{min} is the density of the initial stone (2.65 t/m^3). The reduction factor ϑ may be multiplied by the initial stone size to obtain the corresponding higher density stone size. This term is plausible as there is great similarity with the data driven density term in the formula of Thornton et al. (2014).

Based on the review and evaluation in Abt et al. (2013) the previously presented formulas are assumed to be suitable for the observed conditions in the porotype experiment, and will be used and evaluated against the prototype data. However, one major difference of all between the cited studies to the present case is the temporal scale of the examined load case. All existing formulas are based on stationary flow experiments lasting for 2 to 4 hours per test, incrementally increasing the discharge until failure (Abt and Johnson 1991). However, the overflow due to primary ship waves typically lasts only for up to 30 s, with an even shorter duration of peak discharge. The applicability of the stability relationships for this load thus has to be evaluated using the prototype measurements.

3   Results

In the following, an analysis of the groyne field data presented in Section 2.1 is conducted, utilizing the formulas introduced in Section 2.2 and 2.3.

3.1 Wave – overflowing discharge – relationship

To investigate the relationship between the primary wave and the corresponding overtopping flow, data from B29 V2 (see Table 2) was analysed. In this period an ADV was deployed on the crest in the middle cross-section (see Figure 3), which allowed to analyze the flow and discharge conditions. In the following, a quasi-stationary load case is considered in which the water level on the wave facing side is constant and the overtopping flow is at its maximum (see Figure 5).

The first step in the analysis of the overflowing phenomena is concerned with selecting events from the dataset during which supercritical overflow can be assumed. The indicator for supercritical flow is the depth related Froude number, which is calculated over the groyne crest with following formula:

$$Fr = \frac{v_{crest}}{\sqrt{g \cdot h_{crest}}} \tag{14}$$

All events with a Froude number over unity are considered to be supercritical. From the 1600 analysed primary wave events ultimately 61 events exhibit supercritical flow. The corresponding observed overflowing unit discharge is calculated with:

$$q = h_{crest} \cdot v_{crest} \tag{15}$$

To investigate the relationship between the hydraulic head at the front of the groyne h and the overflowing discharge q, as well as the flow velocity over the crest v_{crest}, each have been plotted in Figure 6. Transforming eq. (1), the weir coefficient μ is calculated for all events with following equation:

$$\mu = \frac{q}{\frac{2}{3}\sqrt{2g \cdot h^3}} \tag{16}$$

From the 61 considered events the mean value of μ is calculated as 0.61 and inserted back in the Poleni equation (eq. 1), resulting in eq. (17). This relationship is plotted in Figure 6 (left). The good fit with the observed data ($R^2 = 0.97$) suggests that the overflow processes on the investigated groyne body cross-sections bear sufficient similarity to weir flow and can be described by means of a modified Poleni formula.

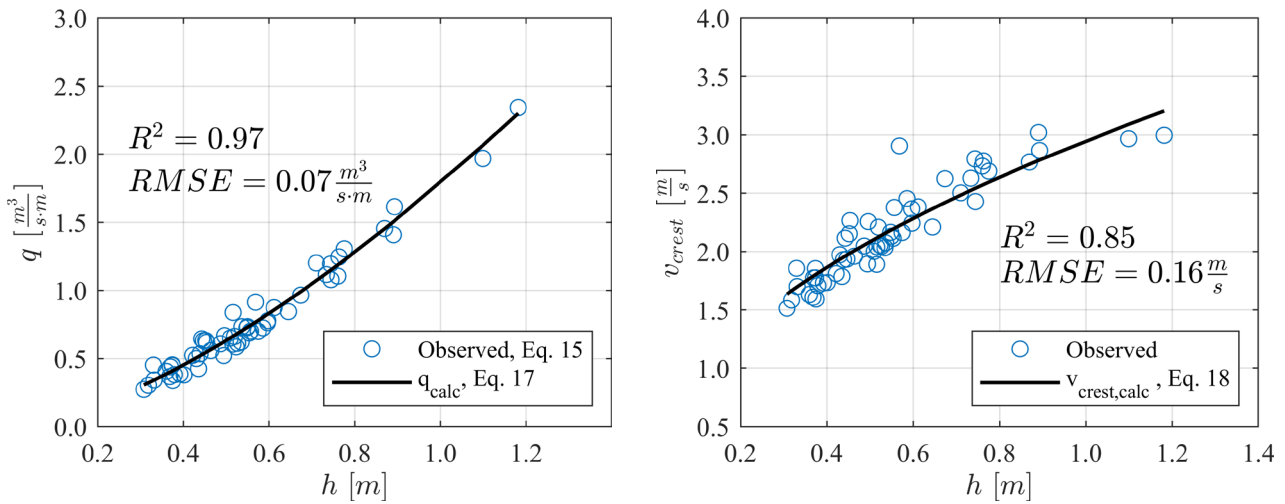$$q_{calc} = 1.80 \cdot h^{\frac{3}{2}} \tag{17}$$

Figure 6: Left: Scatter plot of hydraulic head vs. unit discharge of 61 observed primary wave overtopping events with supercritical overflow for B29 V2. The solid line is the calculated unit discharge using the Poleni formula. Right: Scatter plot of hydraulic head and the observed flow velocity on the groyne crest for the same events. The solid line is the calculated flow velocity using eq. (18).

The weir coefficient μ, which is a measure of the performance of the weir, can be described as ratio of the hydraulic head h in front of the weir and the flow depth at the crest $h_{crest,calc}$ (Peter 2005). This ratio is calculated and averaged to $h_{crest,calc}/h = 0.609$ for the present 61 events. Applying the continuity equation on the flow over the crest and substituting $h_{crest,calc}$ with h and the discharge with eq. (17) results in eq. (18). This formula approximates the flow velocity over the groyne crest using the hydraulic head. This relationship is plotted in Figure 6 (right) and shows good fit ($R^2 = 0.85$) with the observed data:

$$v_{crest,calc} = \frac{q_{calc}}{h_{crest,calc}}$$

$$= \frac{1.80 \cdot h^{\frac{3}{2}}}{0.609 \cdot h} \tag{18}$$

$$= 2.95 \cdot \sqrt{h}$$

Hence, both the overflow discharge and the flow velocity can be described as a function of the hydraulic head, which represents the peak of the stern wave. However, these results refer only to the data from measurement period B29 V2 (see Table 2). To extrapolate these findings to the other groyne and measurement periods, where no ADV is deployed, the ratio of $h_{crest,calc}/h$ is utilized, as it correlates with the weir coefficient μ. Figure 7 shows this relation for every measured overflowing event for all groyne versions. For the values of B29 V2 – with known weir coefficient – a linear regression is performed with 95 % confidence bounds also shown. It is apparent that most values of B29 V1 and B31 (both middle and cross-section) are within this band, which means that the findings developed from the analysis of B29 can be generalized to the other groyne designs and time periods. For the root cross-section of B31 there is a trend towards higher flow depths over the crest for $h > 0.78\ m$. Beside these deviations, the analysis suggests that all groyne profiles have a similar head to discharge relationship and thus a similar weir coefficient. Therefore, the Poleni formula with $\mu = 0.61$ (eq. (17)) and the corresponding flow velocity eq. (18) are utilized in further analysis.
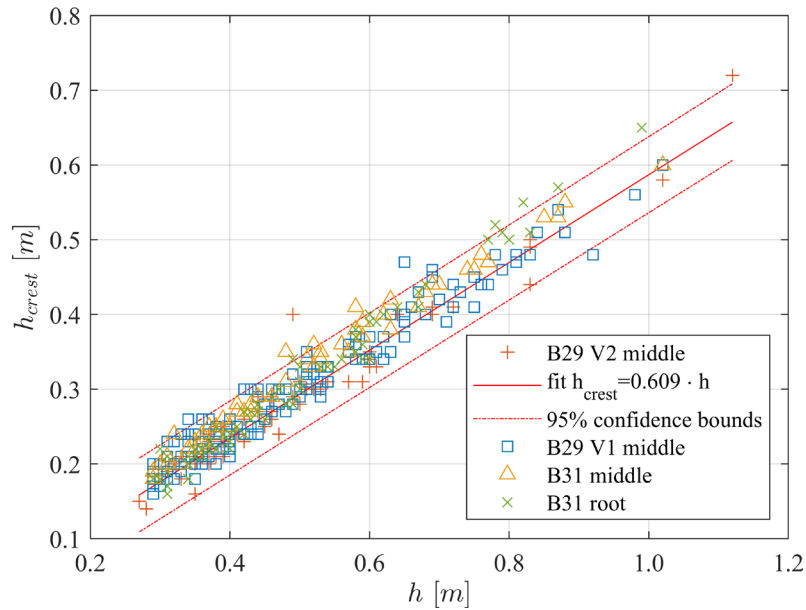
Figure 7: Scatterplot of the hydraulic head against flow depth over the groyne crest for all supercritical overflow events and hydraulic head. The solid line is a linear regression and the dashed lines the corresponding 95 % confidence bounds, both for the values of B29 V2

3.1.1 Influence of leeward water level

An important aspect of the overflowing process concerns the water level on the leeward side of the groyne. As already mentioned in section 2.1, there are no water level measurements on the leeward side for outbound vessels, as pictured in Figure 5. These outbound ships are of particular interest, due to smaller passing distance, which thus generally result in higher loads, as well as more frequent and more significant observed damage. During an overtopping event, the water level on the lee side of the groyne plays a major role as it determines whether supercritical overflow happens. It also influences the length over which the flow can accelerate on the leeward slope and develop a rough bed flow regime. To get a rough estimate of this value for the outbound ship load case, leeward water levels from supercritical overflow events caused from inbound ships have been investigated. However, the number of these events is limited, due to much smaller primary wave magnitudes for inbound ships. This is due to greater passing distance, as well as the fact that inbound ships pass the groynes at higher water levels (compared to outbound ships) due to the tide window for draught-dependent passage to Hamburg as defined in the German Traffic Regulations for Navigable Maritime Waterways.

On the basis of an analysis of water level timeseries from 14 inbound events, a rough estimate of the water level on the leeward side is given in comparison to the water level on the upstream side. At B31, the drawdown is found to be about subsided by half on the downstream side of the groyne, when peak overflow is reached. Whereas, at B29 the drawdown is subsided completely, back to still water level. This difference occurs due to the water flowing through the recessed root area and thus equalizing the water level between the groyne fields faster. With this rough estimation the corresponding downstream slope length L_S can be calculated for each event. To calculate the slope length, which is needed to fully develop rough bed flow, eq. (5) is utilized. As mentioned in section 2.3, the existing riprap stability formulae assume fully developed rough bed flow. However, this condition is not true for events with short observed slope lengths ($L_s < L_d$), where the flow is not fully accelerated and therefor the stress on the riprap is lower. To make these events comparable to fully accelerated flow events ($L_s > L_d$), a new method to adjust these "short slope" events was developed, as described hereafter.

The flow velocity at the groyne crest $v_{crest,calc}$ can be estimated using eq. (18). The fully developed flow velocity v_d on the slope can be calculated using eq. (2). It is now assumed that the flow accelerates linearly between those values. Thus, the adjusted flow velocity v^* can be calculated by linear interpolation based on the ratio of the observed flow length L_s and fully developed flow length L_d:

$$v^*_{calc} = v_{crest,calc} + \frac{L_s}{L_d}(v_{crest,calc} - v_d) \cdot \text{ for } L_s < L_d \tag{19}$$

However, some stability equations utilize the overflowing discharge q as the input parameter. To adjust this discharge, the adjusted velocity v^*_{calc} was entered into the Manning formula eq. (2), which is rearranged to calculate the adjusted flow depth h^*_{calc}:

$$h^*_{calc} = \left(\frac{v^*_{calc}}{k_s \cdot S^{1/2}} \right)^{\frac{3}{2}} \tag{20}$$

The adjusted overflowing discharge can be then calculated using eq. (21). This approach reduces the discharge, which corresponds to a lower stress on the revetment.

$$q^*_{calc} = h^*_{calc} \cdot v^*_{calc} \tag{21}$$

The calculated adjusted velocity and adjusted discharge are plotted in Figure 8 for the root cross-section of B31. When the values of the adjusted velocity or adjusted discharge matches their non-adjusted values, the events have a fully developed and accelerated flow. It can be seen, that high overflow discharge events $q_{calc} > 2.0 \frac{m^3}{s \cdot m}$ occur at high leeward water levels, which lead to short observed slope length L_s and thus result in a large attenuation of the load parameter of up to 30 % the initial discharge.

For further analysis, the calculated v_d and q_{calc} for events with fully developed rough bed flow are used as input parameter for the stability formula. For events with no fully developed rough bed flow the adjusted values v^*_{calc} and q^*_{calc} are used.
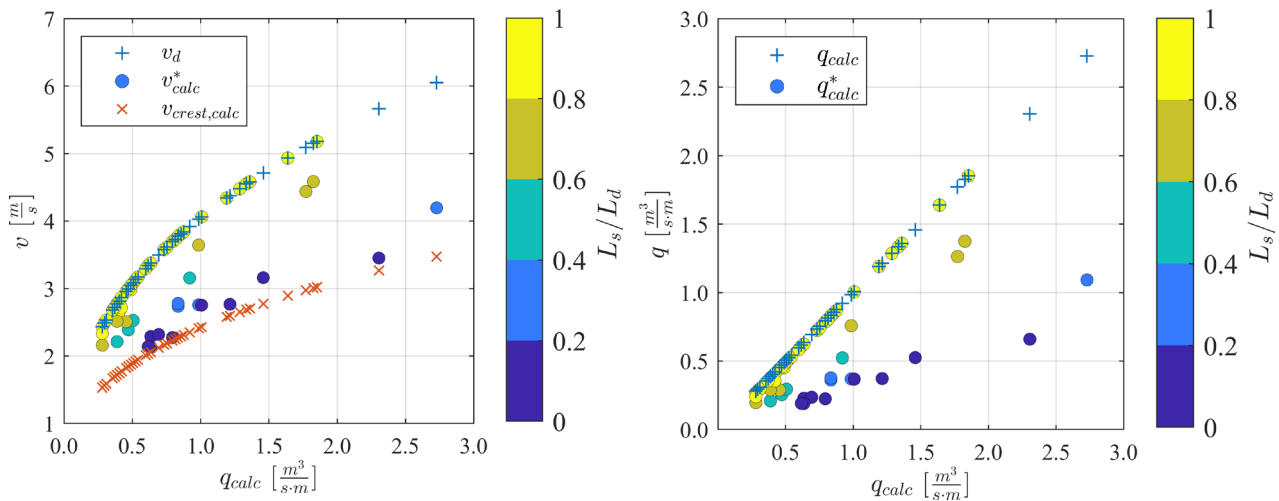

Figure 8: Magnitude of overflow events at B31 root cross-section in comparison to the ratio of observed slope length and fully developed flow length L_s/L_d. Left: Scatter plot of the adjusted velocity v^*_{calc}, the velocity on the groyne crest $v_{crest,calc}$ and the velocity of fully developed flow v_d; Right: Scatter plot of the adjusted overflowing discharge q^*_{calc} in comparison to the calculated overflowing discharge q_{calc}. When the adjusted value is equal to the calculated value, the flow is considered a fully developed rough bed flow.

3.2 Rock sizing

3.2.1 Observed erosion

In order to validate the rock sizing calculations, the entirety of the surface laser scans was examined with the aim of identifying consecutive scans which exhibit rock armour deformation. Due to the level of difficulty in working with this survey data, the evaluation of stone movement was performed visually using difference plots. The information of rock armour deformation is categorized as "erosion" or "no erosion". The "erosion" category is also distinguished into "clear erosion" and "light or local" erosion.

An example is shown in Figure 9, which exhibits two difference plots with each erosion category mentioned before. In the left example, severe damage to the rock armour layer is observed, characterized by erosion along the entire length of the groyne, as well as deposition of the dislodged rocks below. The example on the right shows light erosion, which becomes visible exclusively through deposition, since the laser is not able to detect shallow erosion troughs.
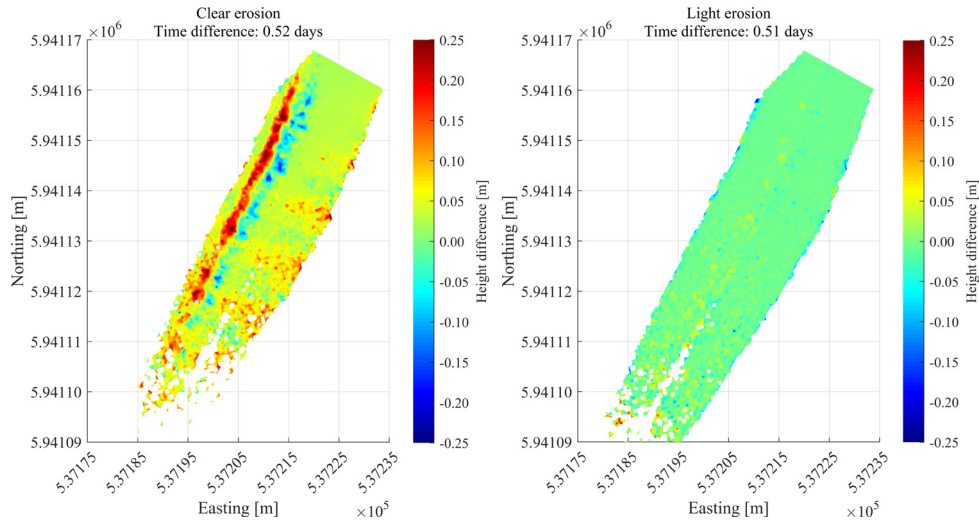

Figure 9: Sample of difference plots derived from laser scan data at B31 (in UTM 32N-ETRS89). Left: Difference plot between two consecutive surveys, showing a clear erosion event, Right: Difference plot between two consecutive surveys, showing a light erosion event.

3.2.2 Evaluation of rock sizing methods

In Figure 10 the calculated stone diameters for all observed overtopping events in the B29 V2 period are plotted using the various stone sizing formulas presented in Section 2.3. The median diameter of the typical stone grading classes from Table 1 are added to the plot. The predicted D_{50} for the different formulas show large variability, which is expected based on the findings of Abt et al. (2013). For the largest observed overflowing event the Formula of Chang (1998) predicted a D_{50} of 0.26 m. The least conservative value is given by the formula of Thornton et al. (2014) which estimated a D_{50} of 0.15 m, which is a 42 % smaller value. The equations by Chang (1998), Olivier (1967) and Abt and Johnson (1991) predict the stone class $LMB_{5/40}$ to be erosive. However, in the B29 V2 period, with $LMB_{5/40}$ in place, no distinct erosion was observed. Therefore, these equations are eliminated from further consideration.
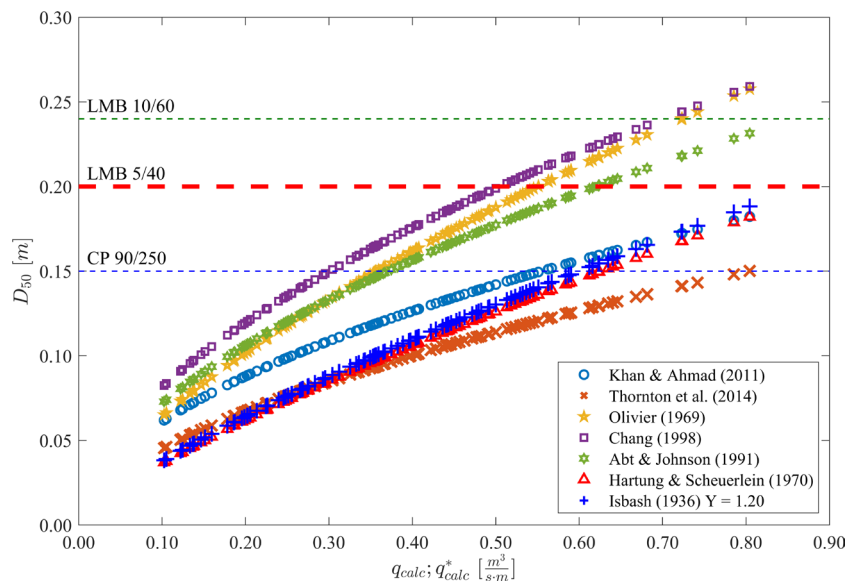

Figure 10: Scatter plot of the calculated stone diameter for each observed overtopping primary wave event using different stone sizing formula. The data is from B29 V2 middle cross-section. The horizontal dashed lines are the median stone sizes of the riprap stone grading classes from Table 1, with the heavy dashed red line being in-situ stone class.

For the final evaluation of the remaining formulas each individual overflowing event and each individual erosion event is considered individually and related to each other. This method is demonstrated in Figure 11 for each groyne variant and cross-section for the stability equation of Thornton et al. (2014). Three quantities are indicated in this figure: the overflowing discharge, the critical discharge calculated from a stability equation and the observed erosion. When an overflowing event exceeds the critical discharge value and corresponds to an observed erosion (located in a red or green area) the erosion event is considered correctly predicted. If there is an observed erosion event but no corresponding over-flowing event, it is considered a missed prediction (false negative). When an overflowing event exceeds the critical value and does not correspond to an observed erosion event, it is considered a false detected erosion event (false positive).

Table 3 summarizes the results of this analysis using the different stability functions. All formulas have a high success rate in predicting the observed erosion events. Concerning the events with a clear erosion pattern, only the formula of Thornton et al. (2014) failed to predict one event in the middle cross section of the B31. Thornton et al. (2014) also yielded the most incorrect predictions of "light or local erosion" events with four, compared to the other formulas, each of which incorrectly predicted two events out of twelve in total. A major difference, however, is the number of false detect events. In total, the formula of Thornton et al. (2014) yielded three events that incorrectly predicted erosion. In contrast, the formula of Isbash (1936) yielded 20, Hartung and Scheuerlein (1970) 22 and Khan and Ahmad (2011) up to 28 false detect events, indicating a possible overestimation of required stone size if these methods were used. Following this analysis, Thornton et al. (2014) is proposed as the best fit formula for the prototype data.

Table 3: Hindcast / Validation of the erosion events prediction using different rock sizing equations

| Riprap stability equation	Erosion event	Correct prediction of an erosive event	Missed prediction of an erosive an event (false negative)	False detect (false positive)
Thornton et al. (2014)	Clear erosion	15	1	3
	Light or local erosion	8	4	
Khan and Ahmad (2011)	Clear erosion	16	0	28
	Light or local erosion	10	2	
Isbash (1936) Y=1.20	Clear erosion	16	0	20
	Light or local erosion	10	2	
Hartung and Scheuerlein (1970)	Clear erosion	16	0	22
	Light or local erosion	10	2	
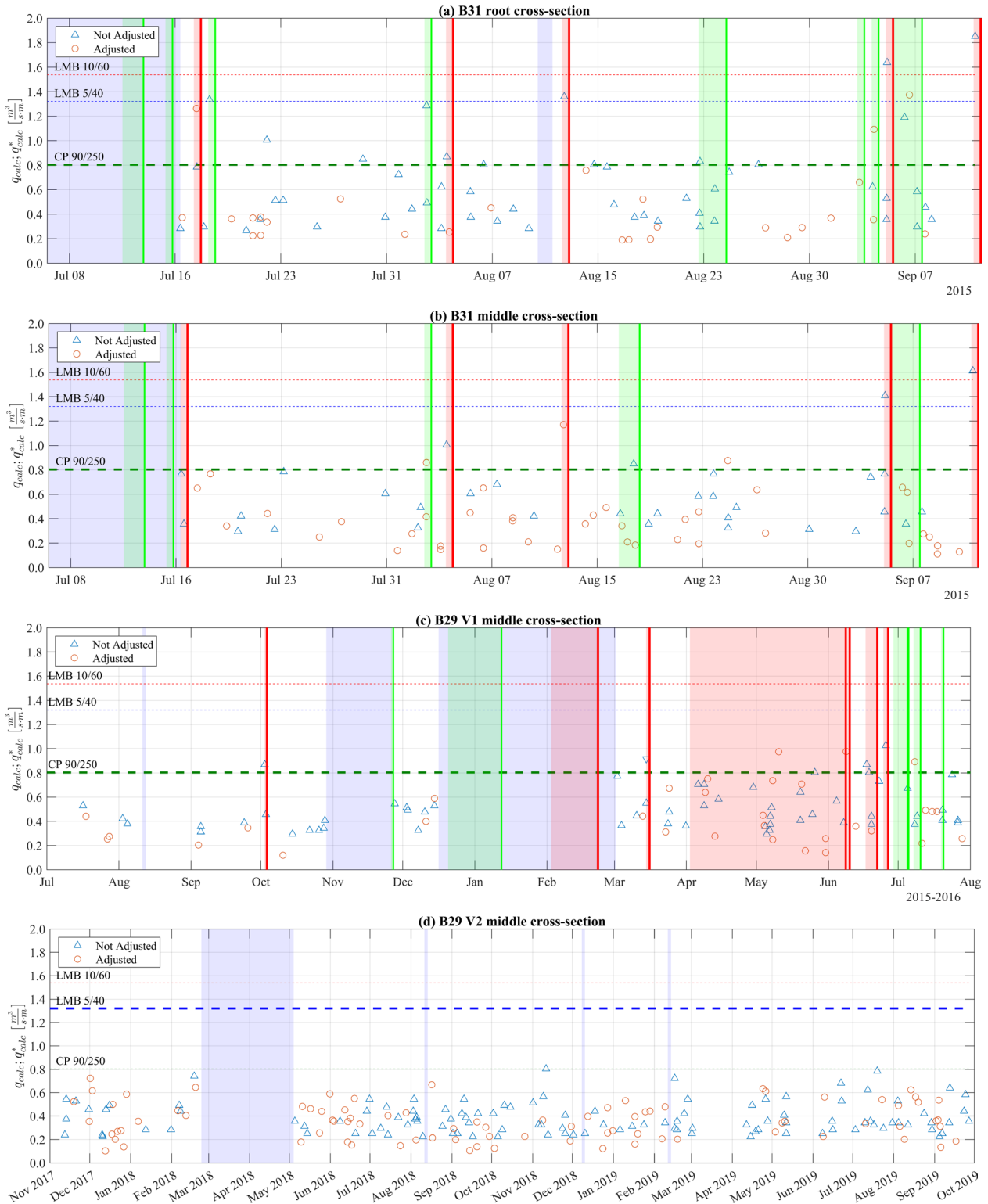
Figure 11: Chronological distribution of the overflowing events. The overflowing events are displayed with markers. The critical discharge using Thornton et al. (2014) is displayed as horizontal dashed lines for the different stone classes in Table 1. The time of the laser survey, where erosion is detected, are displayed as vertical lines, red lines are "clear erosion pattern", green lines "light or local erosion". The green or red areas represent the time to the previous viable scan. Blue areas are time frames, where no wave data was recorded.

4 Discussion

4.1 Factors affecting load intensity

As illustrated in previous sections, the hydraulic head and the downstream water level determine the magnitude of the overflowing discharge. The latter determines the length of exposed leeward slope and thus the effective load length on the rock armour. Both values are dependent on the primary wave height, the drawdown magnitude as well as the ambient water level. Hence, there is a certain "perfect" water level at which the (adjusted) overflow discharge is the largest for a given wave height. When the water level is higher, the leeward slope length becomes shorter and the discharge is reduced. When the water level is lower, the hydraulic head and thus the overflowing discharge becomes smaller. This relationship is pictured in Figure 12 for both groynes. The water level at which the load is largest is associated with a specific overflowing discharge for a specific primary wave height. This discharge is defined as the limit overflowing discharge q_{lim} and is also presented in Figure 12. The intersection between the limit discharge and the critical discharge for each stone grading class is the largest wave height at which the D_{50} will remain stable according to the presented findings. The difference in the slope of q_{lim} between B29 and B31 is due to the different geometry of the groynes. Due to the bypassing of parts of the primary wave through the recess in B29, the water level in the leeward groyne field rises faster compared to the continuous groyne. Thus, the slope length during the overflowing is in generally shorter and thus the load intensity smaller.
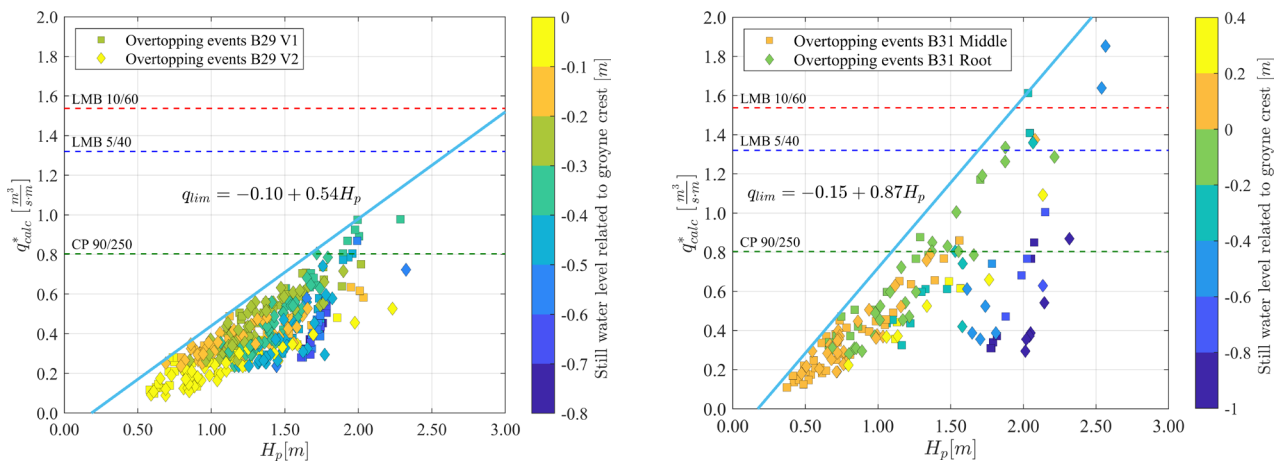

Figure 12: Scatter plots of observed primary wave heights from wave-facing groyne side and the (adjusted) overflowing discharge. Marker colors indicate the still water level in reference to the groyne crest level. Positive values indicate that the groyne is under water before the event. The solid blue line indicates the limit overflowing discharge q_{lim}. Dashed lines are the critical discharges q_c calculated using the formula of Thornton et al. (2014) for stone grading class of Table 1. Left: Middle cross-section of B29 V1 and V2. Right: Event from middle and root cross-section of B31

The previously mentioned wave heights refer to the wave-facing side of the middle and root cross-sections, which correspond to pressure sensors P5 and P4 (cf. Figure 3). These values represent already transformed wave heights. However, the gauge P1 at the groyne tip provides a more undisturbed signal of the primary wave with less structure, bottom or bank interaction. The relationship of the wave heights at the middle and root cross-section to the wave height at the groyne tip are plotted in Figure 13. A good correlation was found between those values, also across both groynes. The wave height in the middle cross-section is around 2.16 times the wave height at the groyne tip. This applies for both B29 V1 and V2, as well as the B31. This suggests that the difference in the shape of the root has little influence on load in the middle of the groyne body. However, the wave transformation at the root of B31 is slightly increased, with a value 2.8 times the initial wave height at the groyne tip. Hence, the load on the root area of the B31 is generally higher than the middle section, which corresponds to the magnitude of the observed discharges and erosion, as the root section eroded faster than in the middle section. As pointed out by Melling et al. (2021) transformation and steepening of the primary wave is affected by structural deterioration. Thus, in Figure 13 for B31 only data from the first 67 days is considered, owing to significant erosion of the groyne crest which alters the hydraulic properties of the groyne with respect to overflow.
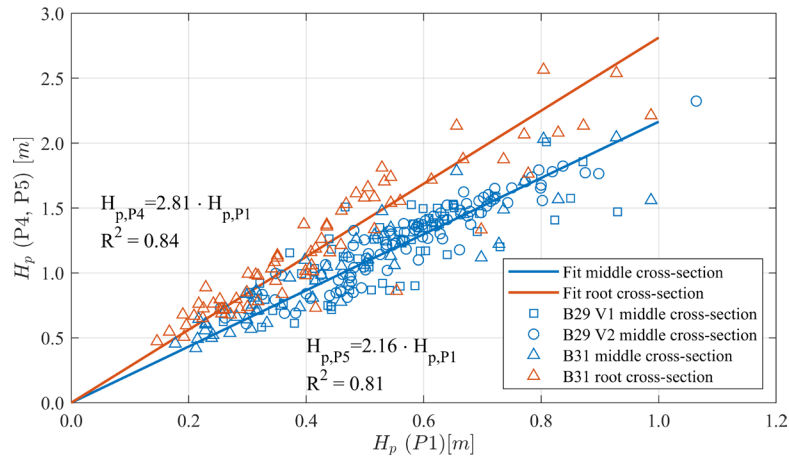
Figure 13: Scatter plot of observed primary wave heights at the groyne tip (P1) in relation to the corresponding wave heights at middle and root cross-sections for both B29 and B31 for overflowing events

As the shape and level of the groyne crest change with the deterioration of the groyne structure, the overflowing discharge relationship changes. This is reflected in the wave data, as the previously used relation of hydraulic head h and flow depth over the crest h_{crest} (see Figure 7) changes significantly past a certain point, as plotted in Figure 14. Subsequent data do not follow the previously described hydraulic relationships.
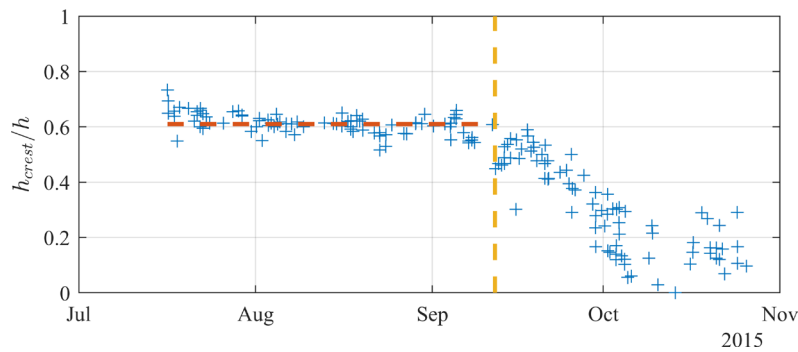

Figure 14: Temporal change of the ratio of flow depth over the crest to hydraulic head for the B31 root section. The vertical dashed line marks the date of the crest breakthrough 67 days after construction. The horizontal dashed line is the mean value before the crest breakthrough.

4.2 Riprap stability equations

The results of the hindcast of the erosion events are presented Section 3.2.2 and summarized in Table 3. All formulas examined were able to predict most of the erosive events. The biggest difference is the number of false detected erosion events. Differences in the underlying experimental parameter space used for the development of these models are thought to play a role in the spread of predictions (cf. Figure 10), as well as inconsistent definitions of riprap failure or stone movement (Thornton et al. 2014). Another reason for the large disparity may be the presence or absence of safety factors in those formulas. Najafzadeh et al. (2017) point out that the formula of Thornton et al. (2014) has a small predictive error and thus little apparent conservatism. However, the same is reported for the formula of Khan and Ahmad (2011), which in contrast, has the most false detects in the present data. This indicates that the latter formula is not appropriate for the conditions in the present case. By collating data from various sources and studies, the parameter space of the composite dataset used for the regression formula of Thornton et al. (2014) is larger and wider spread than that of individual studies, which appears to make it more robust for the present application, as expressed by the best fit with the data. Meanwhile it is important to note that the formula of Thornton et al. (2014) failed to predict one "clear erosive" event. This can be seen as an outlier and a result of the calculation uncertainties, which are discussed later. Yet, the more conservative formulas provide higher safety level, but also the disadvantage of oversizing, which can result in higher effort and cost.

4.3 Evaluation of groyne designs

In the evaluation of the results it is apparent that the magnitude in which the discharge exceeds the critical value has an impact on the magnitude of the erosion. While B29 V1 shows almost as many erosive events as B31 in each considered time period, the observed cumulative erosion is much lower. This can be explained by the overflowing discharge values from the strongest overflowing events. On B29 V1 there is only one event that slightly exceeds a discharge value of $1 \frac{m^3}{s\,m}$, which means that the critical discharge of Thornton et al. (2014) of $q_c = 0.80 \frac{m^3}{s\,m}$ for $CP_{90/250}$ is exceeded by 25 %. At B31 the maximum value of the discharge reached $1.85 \frac{m^3}{s\,m}$, which exceeds the critical value by 130 %. Furthermore, the more frequent occurrence of high-intensity events leads to a rapid deterioration of the rock armour and breakthrough of the groyne crest only 67 days after construction. Several events at B31 also exceed the critical load value for $LMB_{10/60}$ (cf. Figure 11 and Figure 12), indicating that even this larger rock grading may not be stable at B31 under the recorded load conditions at the time.

The smaller load on the recessed groyne B29 compared to the B31 or other continuous groyne has two reasons. The root section allows for wave energy bypassing and dissipation, which means that the area with the highest wave heights in more conventional groyne designs is modified in favour of reduced loading. In addition, the recessed area results in a faster equalization of the water level drawdown in the adjacent groyne field by virtue of the bypass, leading to shorter exposed leeward slop lengths. The recessed groyne design has therefore been proven to offer superior rock armour stability against overflowing long-period primary ship wave loads in comparison to more conventional designs.

In the monitoring period of B29 V2 no apparent erosive event was observed, which is also predicted correctly in the analysis using the Thornton et al. (2014) formula. There are two reasons for this. On the one hand, a coarser rock grading of $LMB_{5/40}$ compared to the previous version was deployed. On the other hand, the implementation of a speed restriction for vessels on the Elbe, which lead to lower extreme primary wave events. The magnitude of the wave height of the top 10 highest events at the groyne tip is reduced by approx. 10 % compared to the previous period without the speed restriction. In these conditions, considering Figure 11d, a rock grading of $CP_{90/250}$ is predicted to be stable, indicating some potential scope for further optimization of the design.

4.4 Proposed method for groyne design

One of the main aims of this paper is the development and validation of a design method to predict the stability of the armour layer exposed to overflowing primary waves. Based on the findings detailed previously, the following workflow is suggested for the design of groynes for ship-induced overflow loads:

1. Determine the design-relevant ship-induced primary wave height at the structure through either prediction or measurement. At existing or prospective groynes, this should be done near the tip of the structure, so that possible bottom induced wave transformation up to that point is considered.

2. Calculate the wave heights along the middle cross-section for recessed groynes or the root area for continuous groynes, using the approach shown in Figure 13. In case of existing groynes it is preferable to measure the wave heights directly at points along those cross-sections, in which case step 1 can be omitted.

3. Determine the overflowing discharge corresponding to the wave height using the equation for the limit discharge q_{lim} proposed in Figure 12. At existing groynes it is preferable to quantify the overflowing discharge from measurements at the structure. In this case, the water level on the leeward side should also be measured, in order to estimate the development of the flow on the slope.

4. Calculate the stone size or the critical overflowing discharge using the stability formula of Thornton et al. (2014).

This workflow would allow a designer to calculate the required stone size, which facilitates a corresponding rock grading to be specified or the stability of an existing structure to be quantified. The stone sizing formula of Thornton et al. (2014) also allows variations of specific riprap design parameters, such as the coefficient of uniformity, the riprap layer thickness, the stone density and the slope angle to be evaluated in terms of their effect on rock armour stability.

However, the findings of the structure-wave-interaction and the overflowing discharge relationship are derived from pro-totype data which only covers a limited parameter space. Caution must hence be exercised when generalizing the pre-sented findings to other groynes, groyne geometries and locations. In the case of the discharge relationship it is possible to either neglect or estimate the effect of a possible change in cross-section geometry. There are many examples for the determination of the weir coefficient and the influence of certain changes in geometries (e.g. Peter 2005). For instance, if the crest of the groyne is wider, a smaller weir coefficient can be assumed. In this case eq. (17) could also be used for added conservatism. The findings of the wave height transformation along the groyne (cf. Figure 13), are valid for the present groynes, as it is purely based on the empirical data. Both groynes have similar dimensions, longitudinal inclina-tion, groyne spacing and beach topography. However, these parameters are expected to have a significant influence on the wave-structure-interaction, as they determine wave focusing, reflection and bottom induced transformation effects. For example, an analysis of aerial images at the site in Juelssand showed that longer groynes started to deteriorate at an earlier time compared to shorter groynes. This suggests that the wave height transformation from Figure 13 may vary for different groyne configurations. Similarly, the lee-side water level can be affected. Nevertheless, the presented findings have given valuable insights into the interaction of long-period ship waves with groyne structures and the proposed design method is a valuable and straightforward tool to estimate the load and the resistance of groynes exposed to primary ship wave overtopping. To counteract the uncertainties arising from extrapolation (to other groynes/locations), safety factors may need to be considered or site-specific measurements conducted.

4.5 Sources of uncertainty

The measurements made in the field experiment as well as the analyses conducted in this paper contain a certain amount of uncertainty. However, all calculations were performed deterministically without taking these uncertainties into account, making a reflection on those necessary. Uncertainties resulting from the measurements are not discussed, al-though they are present and addressed in Melling et al. (2021).

4.5.1 Hydraulic loading assumptions

Most of the uncertainty in the presented analysis arises from required but unmeasured quantities and the assumptions made in order to quantify these. The calculation of the observed discharge q in eq. (15) assumes an equally distributed velocity profile and a hydrostatic pressure distribution over the groyne crest. This is a simplification, as the shape of the groyne is not that of a broad crested weir to which these conditions pertain (Peter 2005). Also, the roughness of the riprap may cause a deformation of the velocity profile (Pařílková et al. 2012). However, both these effects cannot be accounted for due to the point measurements of current velocity and pressure.

To determine the observed hydraulic head h (cf. Figure 5) a crest level had to be defined. As Hiller et al. (2017) points out, the definition of a crest level of a riprap layer to calculate the water level is somewhat arbitrary. For the calculations in this paper it was defined as the outer edges of the rocks of the riprap layer. With large values overflowing height of $2.4 \le h_{crest}/D_{50} \le 5.2$ for erosive overflowing events, the current in the direct proximity of the riprap layer is assumed to be insignificant.

Also, the influence of the approach velocity v_0 on the overflowing process could not be considered due to the lack of measurement of this parameter. In the analysis of Aigner (2008) the approach energy is determined by the relation of hydraulic head and weir height. Based on this, the difference in discharge of an infinite weir height ($h/w \to 0$) compared to observed erosive overflowing event at the groynes with values of $0.3 \le h/w \le 0.5$ resides at 1.5 % to 3.0 %. This influence can therefore be considered to be rather small.

In the processing of the primary wave, higher frequency components (> 0.1 Hz) are filtered out. However, during an overtopping event secondary waves may interfere or superimpose on the primary wave. The effect of these secondary waves on the overtopping discharge is estimated to be low and was neglected. This is in line with EurOtop (2018), which rates wave heights of smaller than three times the hydraulic head as negligible in the calculation of the overflowing discharge for the case of stationary overflowing of dikes.

However, all the above-mentioned assumptions and uncertainties are incorporated in the weir coefficient that is cal-culated from the observed events in eq. (16). Further investigations and more complex methods may provide an even

better picture of the individual physical effects related to this discharge relationship. However, the approach at hand is in good agreement with the data and thus a sound estimator for the present hydraulic conditions.

The developed method of adjusting the leeward slope flow velocity and overflowing discharge using eq. (19) and eq. (21) to consider the impact of the leeward water level is considered speculative. There are major uncertainties in the calculation of the development of the boundary layer using eq. (4), as the variance term of this equation suggests. Also, the assumption of linear acceleration used in eq. (19) may not represent the actual conditions. The reduction of the discharge to assess those events is subject to major uncertainties. However, this approach is meant to acknowledge the lower stress on the riprap by corresponding to the reduced velocity. This procedure cannot be validated with the available data. As pointed out earlier, these calculations were done in order to assess events with a relative short lee-slope length and thus to evaluate all observed erosion events.

The influence of interstitial flow in the riprap layer was omitted, due to the seemingly small proportion compared to the overflowing discharge (Hiller et al. 2018) and the lack of measurements.

4.5.2 Stationary flow assumption

The findings in this paper were conducted under the assumption of a quasi-stationary flow at the time at which the overflowing surge is at its maximum. Thus, the time dependency of the wave and the overflowing process are not considered. This has possible implications on the wave-overflow relationship and the erosion process.

Figure 15 shows an example overflowing event as represented by measurements of the water level and flow velocity. Additionally, the flow velocity and the overflowing discharge are calculated using eq. (17) and eq. (18). It can be concluded that both the shape and the magnitude of the calculated parameter curves agree with the observations over the course of the wave. This suggests that the assumption and thus the proposed equations are adequate approximations of the observed time dependent processes.

The erosion analysis in section 3.2.2 is based on the initial stone movement, which is correlated with a critical discharge. Hence, only the start of motion is considered and the quasi-stationary information seems to be sufficient to assess this information. Time dependent information could allow for the calculation of erosion rates or erosion volumes. This was, however, not in the scope of the paper. Dynamic pore pressure variations in the groyne core were not considered, as no geotechnical failure mechanisms are observed in conjunction with the primary wave load.
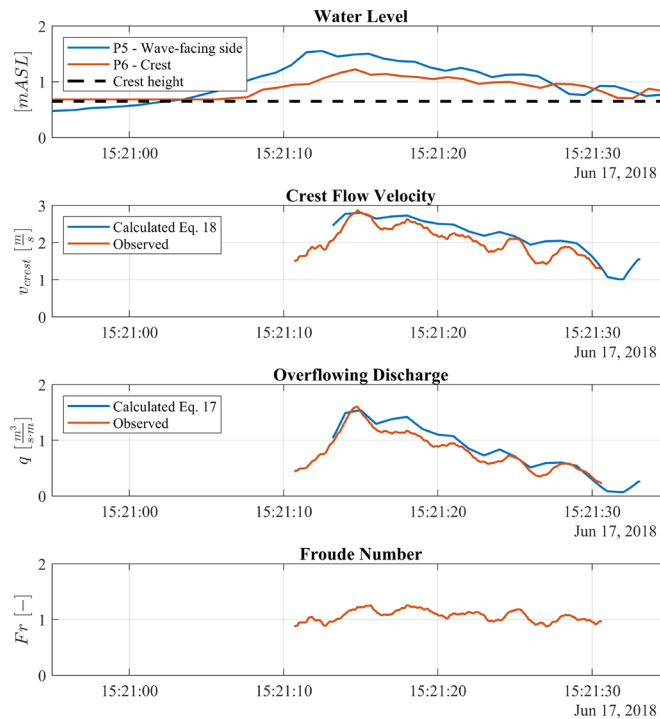

Figure 15: Pressure sensor timeseries at B29 V2 middle cross-section of single observed primary ship wave event, crest flow velocity, overflow discharge and Froude number

5 Conclusions

In this paper, an analysis of data from a groyne prototype experiment was conducted in order to derive a workflow for rock sizing for groynes subject to ship-induced overflow loads. In reference to the aims raised in the introduction, the following conclusions can be drawn.

Existing formulae for weir overflow, rough bed flow and riprap exposed to overtopping, are appropriate to describe the interrelationships between the primary wave load, overflow discharge and the resulting riprap erosion. The calculations were reliable for a continuous and a recessed groyne. From 16 clear erosive events 15 could be predicted correctly, while having only three false predicted events.

1. Besides the wave height, the water level in reference to the groyne crest appeared to be a deciding factor for the occurrence and intensity of supercritical overflowing process. A method to gauge overflowing events with limited leeward slope length was developed. However, it could not be validated due to the lack of appropriate measurements.

2. The consideration of the flow as quasi-stationary seemed to fit the data sufficiently well. However, the influence of the dynamic behaviour of the primary ship wave has yet to be examined.

3. Based on the findings in this paper, a workflow for the rock sizing of groynes exposed to long-period ship waves is presented. As it is based on finite empirical data, generalization has to be done prudently.

We recommend further research to generalize findings for different groyne geometries and wave properties. Numerical modelling or laboratory experiments appears to be best suitable to investigate the wave-structure-interaction for a variety of configurations. In this context, important assumptions of this paper can also be validated. Especially, the assumptions about the leeward water level during the overflowing event and corresponding adjustment of the flow velocity and the discharge contain major uncertainties, which yet have to be resolved.

Notation

Name	Symbol	Unit
Median stone diameter	D_{50}	cm
Coefficient of uniformity	C_u	-
Stone density	ρ_s	t/m³
Weir coefficiant	μ	-
Hydraulic head	h	m
Observed flow depth on the groyne crest	h_{crest}	m
Observed flow velocity on the groyne crest	v_{crest}	m/s
Observed overflowing discharge	q	$\frac{m^3}{s\,m}$
Depth related Froude number	Fr	-
Critical overflowing discharge	q_c	$\frac{m^3}{s\,m}$
Approach velocity	v_0	m/s
Observed exposed slope length	L_S	m
Flow depth at fully developed rough bed flow	h_d	m
Flow velocity at fully developed rough bed flow	v_d	m/s
Flow length required to fully develop the boundary layer	L_d	m
Slope inclination	S	-
Calculated flow depth on the groyne crest	$h_{crest,calc}$	m

Calculated flow velocity on the groyne crest	$v_{crest,calc}$	m/s
Calculated overflowing discharge	q_{calc}	$\frac{m^3}{s\,m}$
Calculated adjusted flow depth on the groyne crest	h^*_{calc}	m
Calculated adjusted flow velocity on the groyne crest	v^*_{calc}	m/s
Calculated adjusted overflowing discharge	q^*_{calc}	$\frac{m^3}{s\,m}$
Primary wave height	H_p	m
Groyne height	w	m

Acknowledgements

Author contributions (CRediT)

AS: writing – original draft and editing, investigation, methodology, formal analysis, visualization: GM – review and editing, conceptualization, supervision; HJ: data acquisition, data processing; BK data acquisition, data processing;

References

Abt, S.R.; Ruff, J.F.; Wittler, R.J.; LaGrone, D.L. (1987): Gradiation and Layer Thickness Effects on Riprap. Proceedings of the National Conference on Hydraulic Engineering ASCE, pp. 564-575.

Abt, Steven R.; Johnson, Terry (1991): Riprap Design for Overtopping Flow. In *Journal of Hydraulic Engeneering* 117 (8), pp. 959–972.

Abt, Steven R.; Thornton, Christopher I.; Scholl, Bryan A.; Bender, Theodore R. (2013): Evaluation of Overtopping Riprap Design Relationships. In *JAWRA Journal of the American Water Resources Association* 49 (4), pp. 923–937. DOI: 10.1111/jawr.12074.

Aigner, Detlef (2008): Überfälle (Overfalls). In *Dresdner Wasserbauliche Mitteilungen* (36). Available online at http://rcswww.urz.tu-dresden.de/~daigner/pdf/ueberf.pdf.

Bertram, Volker (2002): Practical ship hydrodynamics. Reprint. Oxford: Butterworth-Heinemann.

Bhowmik, Nani G.; Demissie, Misganaw; Guo, Chwen-Yuan (1982): Waves Generated by River Traffic and Wind on the Illinois and Mississippi Rivers.

Chang, H. H. (1998): Riprap stability on steep slopes. In *Int. J. Sediment Res.* 13 (2), pp. 40–49.

CIRIA (2007): The Rock Manual. The use of rock in hydraulic engineering. The use of rock in hydraulic engineering. Centre d'études maritimes et fluviales (CETMEF), Civieltechnisch Centrum Uitvoering Research en Regelgeving (CUR), Construction Industry Research and Information Association (CIRIA), 2. ed. London.

Dempwolff, León-Carlos; Melling, Gregor; Windt, Christian; Lojek, Oliver; Martin, Tobias; Holzwarth, Ingrid et al. (2022): Loads and effects of ship-generated, drawdown waves in confined waterways - A review of current knowledge and methods. 46 Pages / Journal of Coastal and Hydraulic Structures, Vol. 2 (2022). DOI: 10.48438/JCHS.2022.0013.

Esteban, Miguel; Glasbergen, Toni; Takabatake, Tomoyuki; Hofland, Bas; Nishizaki, Shinsaku; Nishida, Yuta et al. (2017): Overtopping of Coastal Structures by Tsunami Waves. In *Geosciences* 7 (4), p. 121. DOI: 10.3390/geosciences7040121.

EurOtop (2018): Manual on wave overtopping of sea defences and related structures. An overtopping manual largely based on European research, but for worldwide application. Van der Meer, J.W., Allsop, N.W.H., Bruce, T., De Rouck, J., Kortenhaus, A., Pullen, T., Schüttrumpf, H., Troch, P. and Zanuttigh, B., www.overtopping-manual.com.

GBB (2010): Principles for the Design of Bank and Bottom Protection for Inland Waterway (BAW Code of Practice). Bundesanstalt für Wasserbau.

Gier, Fabian; Schüttrumpf, Holger (2012): Schiffserzeugte langperiodische Belastung zur Bemessung der Deckschichten von Strombauwerken an Seeschifffahrtsstraßen. AP2 – Wissenstandanalyse der an der Wellen-Strombauwerk-Interaktion beteiligten Belastungsprozesse. [Report, unpublished]. Lehrstuhl und Institut für Wasserbau und Wasserwirtschaft, RWTH Aachen.

Hartung, D.C.; Scheuerlein, H (1970): Design of Overflow Rock-fill Dams. Proceedings of the 10th International Congress of Large Dams 1:587-598.

Hiller, Priska H.; Aberle, Jochen; Lia, Leif (2017): Displacements as failure origin of placed riprap on steep slopes. In *Journal of Hydraulic Research* 56 (2), pp. 141–155. DOI: 10.1080/00221686.2017.1323806.

Hiller, Priska H.; Lia, Leif; Aberle, Jochen (2018): Field and model tests of riprap on steep slopes exposed to overtopping. In *Journal of Applied Water Engineering and Research* 7 (2), pp. 103–117. DOI: 10.1080/23249676.2018.1449675.

Houser, Chris (2011): Sediment Resuspension by Vessel-Generated Waves along the Savannah River, Georgia. In *J. Waterway, Port, Coastal, Ocean Eng.* 137 (5), pp. 246–257. DOI: 10.1061/(ASCE)WW.1943-5460.0000088.

Isbash, S.V. (1936): Construction of dams by depositing rock in running water. Second congress on large dams. Washington, DC, 1936, pp. 126–136.

Khan, D.; Ahmad, Z. (2011): Stabilization of Angular-Shaped Riprap under Overtopping Flows. In *International Journal of Civil and Environmental Engineering* 5 (11).

Kurdistani, Sahameddin Mahmoudi; Tomasicchio, Giuseppe R.; D'Alessandro, Felice; Hassanabadi, Leila (2019): River bank protection from ship-induced waves and river flow. In *Water Science and Engineering* 12 (2), pp. 129–135. DOI: 10.1016/j.wse.2019.05.002.

Melling, Gregor; Jansch, Hanne; Kondziella, Bernhard; Uliczka, Klemens; Gätje, Bettina (2019): Damage to Rock Groynes from Long-Period Ship Waves: Towards a Probabilistic Design Method. Edited by Nils Goseberg, Schlurmann, Torsten: Coastal Structures 2019. Karlsruhe: Bundesanstalt für Wasserbau. pp. 10–19. Available online at DOI: 10.18451/978-3-939230-64-9_002.

Melling, Gregor; Jansch, Hanne; Kondzielle, Bernhard; Uliczka, Klemens; Gätje, Bettina (2021): Evaluation of optimised groyne designs in response to long-period ship wave loads at Juelssand in the Lower Elbe Estuary. In *Die Küste* 89, pp. 29–56. DOI: 10.18171/1.089103.

Muscalus, A.C.; Haas, K.A. (2022): Vessel wake contributions to erosion at exposed and sheltered shorelines near a tidal shipping channel. In *Coastal engineering* 178, p. 104220. DOI: 10.1016/j.coastaleng.2022.104220.

Najafzadeh, Mohammad; Rezaie-Balf, Mohammad; Tafarojnoruz, Ali (2017): Prediction of riprap stone size under overtopping flow using data-driven models. In *International Journal of River Basin Management* 16 (4), pp. 505–512. DOI: 10.1080/15715124.2018.1437738.

Olivier, H. (1967): Through and overflow rock fill dams – new design techniques. In *Proceedings of the Institution of Civil Engineers* 36 (3), pp. 433–471.

Parílková, Jana; Říha, Jaromír; Zachoval, Zbyněk (2012): The Influence of Roughness on the Discharge Coefficient of a Broad-Crested Weir. In *Journal of Hydrology and Hydromechanics* 60 (2), pp. 101–114. DOI: 10.2478/v10098-012-0009-0.

Parnell, Kevin E.; Soomere, Tarmo; Zaggia, Luca; Rodin, Artem; Lorenzetti, Giuliano; Rapaglia, John; Scarpa, Gian Marco (2015): Ship-induced solitary Riemann waves of depression in Venice Lagoon. In *Physics Letters A* 379 (6), pp. 555–559. DOI: 10.1016/j.physleta.2014.12.004.

Pells, Steven E.; Peirson, William L. (2015): Discussion. "Evaluation of Overtopping Riprap Design Relationships". In *J Am Water Resour Assoc* 51 (2), pp. 569–572. DOI: 10.1111/jawr.12260.

Peter, Günter (2005): Überfälle und Wehre (Overflowing structures and Weirs). Wiesbaden: Friedr. Vieweg & Sohn Verlag.

Platzer, G. (1983): Die Hydraulic der breiten Blocksteinrampe - eine Bemesungsgrundlage (Hydraulics of broad rock chutes - design principles). Budesanstalt für Wasserbauversuche und hydrometrische Prüfung. Wien.

Rapaglia, John; Zaggia, Luca; Parnell, Kevin; Lorenzetti, Giuliano; Vafeidis, Athanasios T. (2015): Ship-wake induced sediment remobilization: Effects and proposed management strategies for the Venice Lagoon. In *Ocean & Coastal Management* 2015 (110), pp. 1–11 DOI: 10.1016/j.ocecoaman.2015.03.002.

Robinson, K. M.; Rice, C. E.; Kadavy, K. C. (1998): Design of Rock Chutes. Australia. Robinson, K.M., C.E. Rice, and K.C. Kadavy,. In *Transactions of the American Society of Agricultural Engineers* 41 (3), pp. 621–626.

Schiereck, G. (2001): Introduction to Bed, Bank and Shore Protection. 1st ed. Delft, The Netherlands: Delft University Press.

Schoellhamer, David H. (1996): Anthropogenic Sediment Resuspension Mechanisms in a Shallow Microtidal Estuary. In *Estuarine, Coastal and Shelf Science* 43 (5), pp. 533–548. DOI: 10.1006/ecss.1996.0086.

Schroevers; Huisman; van der Wal, Terwindt (2011): Measuring ship induced waves and currents on a tidal flat in the Western Scheldt Estuary. 2011 IEEE/OES 10th current, waves and turbulence measurements (CWTM 2011), Monterey, California, USA, 20 - 23 March 2011; [conference proceedings].

Soomere, Tarmo (2007): Nonlinear Components of Ship Wake Waves. In *Applied Mechanics Reviews* 60 (3), pp. 120–138. DOI: 10.1115/1.2730847.

Thornton, Christopher I.; Abt, Steven R.; Scholl, Bryan N.; Bender, Theodore R. (2014): Enhanced Stone Sizing for Overtopping Flow. In *J. Hydraul. Eng.* 140 (4), p. 6014005. DOI: 10.1061/(ASCE)HY.1943-7900.0000830.

van der Meer, J. W. (1988): Rock Slopes and Gravel Beaches under Wave Attack. Delft Hydraulics Communication No. 396.

Verhey, H.J.; Bogaerts, M.P. (1989): Ship waves and the stability of armour layers protecting slopes. 9th International Harbour Congress; Antwerp, Belgium, June1989; Delft Hydraulics Publication No. 428.

Zaggia, Luca; Lorenzetti, Giuliano; Manfé, Giorgia; Scarpa, Gian Marco; Molinaroli, Emanuela; Parnell, Kevin Ellis et al. (2017): Fast shoreline erosion induced by ship wakes in a coastal lagoon: Field evidence and remote sensing analysis. In *PloS one* 12 (10), e0187210. DOI: 10.1371/journal.pone.0187210.